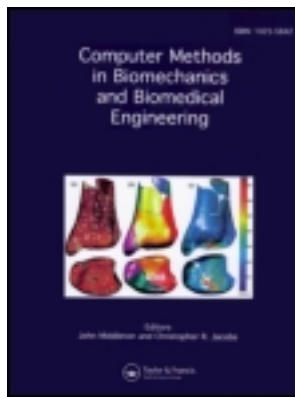


This article was downloaded by: [171.65.65.46]

On: 12 February 2013, At: 21:13

Publisher: Taylor & Francis

Informa Ltd Registered in England and Wales Registered Number: 1072954 Registered office: Mortimer House, 37-41 Mortimer Street, London W1T 3JH, UK



Computer Methods in Biomechanics and Biomedical Engineering

Publication details, including instructions for authors and subscription information:
<http://www.tandfonline.com/loi/gcmb20>

Characterisation of electrophysiological conduction in cardiomyocyte co-cultures using co-occurrence analysis

Michael Q. Chen ^a, Jonathan Wong ^b, Ellen Kuhl ^{a b}, Laurent Giovangrandi ^c & Gregory T.A. Kovacs ^c

^a Department of Bioengineering, Stanford University, Stanford, CA, 94305, USA

^b Department of Mechanical Engineering, Stanford University, Stanford, CA, 94305, USA

^c Department of Electrical Engineering, Stanford University, Stanford, CA, 94305, USA

Version of record first published: 04 Oct 2011.

To cite this article: Michael Q. Chen , Jonathan Wong , Ellen Kuhl , Laurent Giovangrandi & Gregory T.A. Kovacs (2013): Characterisation of electrophysiological conduction in cardiomyocyte co-cultures using co-occurrence analysis, Computer Methods in Biomechanics and Biomedical Engineering, 16:2, 185-197

To link to this article: <http://dx.doi.org/10.1080/10255842.2011.615310>

PLEASE SCROLL DOWN FOR ARTICLE

Full terms and conditions of use: <http://www.tandfonline.com/page/terms-and-conditions>

This article may be used for research, teaching, and private study purposes. Any substantial or systematic reproduction, redistribution, reselling, loan, sub-licensing, systematic supply, or distribution in any form to anyone is expressly forbidden.

The publisher does not give any warranty express or implied or make any representation that the contents will be complete or accurate or up to date. The accuracy of any instructions, formulae, and drug doses should be independently verified with primary sources. The publisher shall not be liable for any loss, actions, claims, proceedings, demand, or costs or damages whatsoever or howsoever caused arising directly or indirectly in connection with or arising out of the use of this material.

Characterisation of electrophysiological conduction in cardiomyocyte co-cultures using co-occurrence analysis

Michael Q. Chen^a, Jonathan Wong^b, Ellen Kuhl^{a,b*}, Laurent Giovangrandi^c and Gregory T.A. Kovacs^c

^aDepartment of Bioengineering, Stanford University, Stanford, CA 94305, USA; ^bDepartment of Mechanical Engineering, Stanford University, Stanford, CA 94305, USA; ^cDepartment of Electrical Engineering, Stanford University, Stanford, CA 94305, USA

(Received 13 May 2011; final version received 15 August 2011)

Cardiac arrhythmias are disturbances of the electrical conduction pattern in the heart with severe clinical implications. The damage of existing cells or the transplantation of foreign cells may disturb functional conduction pathways and may increase the risk of arrhythmias. Although these conduction disturbances are easily accessible with the human eye, there is no algorithmic method to extract quantitative features that quickly portray the conduction pattern. Here, we show that co-occurrence analysis, a well-established method for feature recognition in texture analysis, provides insightful quantitative information about the uniformity and the homogeneity of an excitation wave. As a first proof-of-principle, we illustrate the potential of co-occurrence analysis by means of conduction patterns of cardiomyocyte–fibroblast co-cultures, generated both *in vitro* and *in silico*. To characterise signal propagation *in vitro*, we perform a conduction analysis of co-cultured murine HL-1 cardiomyocytes and murine 3T3 fibroblasts using microelectrode arrays. To characterise signal propagation *in silico*, we establish a conduction analysis of co-cultured electrically active, conductive cardiomyocytes and non-conductive fibroblasts using the finite element method. Our results demonstrate that co-occurrence analysis is a powerful tool to create purity–conduction relationships and to quickly quantify conduction patterns in terms of co-occurrence energy and contrast. We anticipate this first preliminary study to be a starting point for more sophisticated analyses of different co-culture systems. In particular, in view of stem cell therapies, we expect co-occurrence analysis to provide valuable quantitative insight into the integration of foreign cells into a functional host system.

Keywords: electrophysiology; microelectrode arrays; finite element method; cardiomyocytes; texture analysis; pattern recognition

1. Introduction

Cardiac arrhythmias are common heart disorders that can lead to severe complications, making them a significant area of research (American Heart Association 2010). In the healthy heart, rhythmic contraction is initiated by the generation of an action potential by a group of pacemaker cells, resulting in the depolarisation of their neighbouring cells, and, consequently, in the formation of an excitation wave (Kotikanyadanam et al. 2010). This process provides the basis for the unimpeded smooth propagation of depolarisation across the heart (Kleber and Rudy 2004). Some cardiac conditions such as ischaemia (Janse and van Capelle 1982; Johnston 2010) or infarction (Tsai et al. 2000) can lead to changes in tissue structure associated with the formation of non-conductive fibrous tissue (Kohl et al. 2005). Non-functional regions may vary in size and shape, but even small areas of damage can lead to severe disruption of the conduction system and initiate cardiac arrhythmias (Smith et al. 1991).

An emerging cause of arrhythmias is cell injection therapy (Chang et al. 2006; Wenk et al. 2011). This relatively new technique to restore functional tissue within a damaged heart (Patel et al. 2005) may introduce

complications in conduction since the electrical properties of the newly added cells may not match those of the host tissue (Chen et al. 2010; Abilez, Wong et al. 2011). Heterogeneous cell populations, resulting either from impure stem cell-derived populations or from diffuse integration within the host, may further increase the risk of arrhythmias rather than improve regeneration and repair (Cao et al. 2006; Abilez, Baugh et al. 2011). For cell injection therapies to be successful, it is therefore essential to understand the relationship between tissue homogeneity and smooth signal propagation (Kehat et al. 2004). We hypothesise that a minimum volume fraction of electrically active cells must be present to support the propagation of a uniform, smooth depolarisation wave.

To investigate purity–conduction relationships in electrically active tissue, various different *in vitro* models (Gaudesius et al. 2003; Camelliti et al. 2005) and *in silico* models (Krinsky 1978; Zlochiver et al. 2008) have been proposed to complement *in vivo* studies in small and large animals (Janse et al. 1998; Kehat et al. 2004). In contrast to *in vivo* models, *in vitro* and *in silico* models allow us to combine conductive and non-conductive cells under reproducible, well-controlled conditions (Rook et al.

*Corresponding author. Email: ekuhl@stanford.edu

1992; Miragoli et al. 2006). They can indicate trends of conduction patterns and are widely accepted approaches to characterise the electrophysiology of pure cell populations and of co-cultures of different cell types (Xie et al. 2009). In view of stem cell therapies, optical mapping of mixed cultures of neonatal rat ventricular myocytes and mesenchymal stem cells has demonstrated the merit of *in vitro* models for studying arrhythmogenesis (Chang et al. 2006). Although this study provides general first insight, it requires cytotoxic dyes and is therefore unsuitable for long-term culture. More importantly, the demonstration of pro-arrhythmic potential presented in this study is not quantitative. In order to study the arrhythmogenic risk associated with stem cell transplantation, there is a clear need for quantitative metrics that assess conduction patterns in a repeatable, efficient and comparable fashion.

The objective of this study was to establish an easily reproducible method to generate purity–conduction relationships for co-culture systems with different volume fractions. To illustrate the features of this method, we analyse conduction patterns of cardiomyocyte–fibroblast co-cultures generated both *in vitro* and *in silico*. For the *in vitro* conduction analysis, we study co-cultured murine HL-1 cardiomyocytes and murine 3T3 fibroblasts using microelectrode arrays (MEAs). For the *in silico* analysis, we explore co-cultured electrically active, conductive cardiomyocytes and non-conductive fibroblasts using the finite element method (FEM). To quantify conduction patterns and to compare the results of the *in vitro* and *in silico* analyses, we establish a novel method, the co-occurrence analysis of local activation times (LATs). We illustrate how to create co-occurrence matrices for co-cultures with systematically varying cardiomyocyte-to-fibroblast ratios. To quickly portray the pattern of a depolarisation wave, we extract two scalar-valued quantities from the co-occurrence matrix: co-occurrence energy and co-occurrence contrast. In a first proof-of-principle study, we find that both values indicate a significant disturbance of smooth, uniform conduction at cardiomyocyte-to-fibroblast ratios of 80:20. At ratios below the critical threshold of 50:50, we observe a complete loss of the electrical signal.

2. Methods

2.1 In vitro conduction analysis using MEAs

To characterise the action potential propagation in cardiomyocyte–fibroblast co-cultures *in vitro*, we acquire activation sequences using MEA recordings.

2.1.1 Cell culture

We use murine atrial tumorigenic HL-1 cardiomyocytes as an electrically active, conductive host system (Claycomb

et al. 1998). We culture HL-1 cardiomyocytes in Claycomb media (Sigma-Aldrich, St. Louis, MO, USA) supplemented with 10% fetal bovine serum (FBS, Hyclone, Logan, UT, USA), 100 mM norepinephrine (Sigma-Aldrich), 100 units/ml penicillin streptomycin (Invitrogen, Carlsbad, CA, USA) and 4 mM L-glutamine (Invitrogen). The HL-1 cardiomyocytes undergo mitosis approximately every 18 h. When cultured to confluence, they are capable of beating spontaneously at a rate of 60–180 beats per minute. To block conduction pathways, we use murine 3T3 fibroblasts as a non-conductive cell type. Our fibroblast media consists of a solution containing 89% DMEM (Invitrogen), 10% FBS (Hyclone) and 1% penicillin–streptomycin (Invitrogen). To establish quantitative purity–conduction relationships, we create 21 different co-cultures with a cardiomyocyte-to-fibroblast ratio varying from 100:0 to 0:100 in increments of 5. For each cardiomyocyte-to-fibroblast ratio, we analyse $n = 3$ samples. To confirm different cardiomyocytes-to-fibroblast ratios and to validate the co-culture method, we transfect our HL-1 cardiomyocytes with a green fluorescent protein (GFP) marker through the lentiviral vector LentiLox PLL3.7 (Rubinson et al. 2003). We plate the samples on a 35-mm Petri dish adhered to the circuit board with our MEA using bio-compatible epoxy (EP42HT, Master Bond; Hackensack, NJ, USA).

2.1.2 Microelectrode array

To record electrical signal propagation, we utilise 36 microelectrodes arrayed in a 6×6 square on a glass substrate (Whittington et al. 2005). Our microelectrodes are 22 μm in diameter and spaced 100 μm apart, covering a total area of $500 \times 500 \mu\text{m}^2$ as shown in Figure 1(A) and (B). This set-up is capable to monitor the electrical activity of various different cell types in real time over the course of several days (Whittington and Kovacs 2008). We acquire MEA data from 32 channels, excluding the four corner electrodes. Using a custom recording system that consisted of a 32-channel amplifier with a two-stage gain of 60 dB, 7 Hz first-order high-pass cut-off and 3 kHz eighth-order low-pass cut-off, we process the signals as previously reported (Gilchrist et al. 2001). We digitise the analog signals from the amplifier board with 16-bit resolution at 10 kbps using a custom-designed visualisation and extraction tool written in Matlab (The MathWorks; Natick, MA; Whittington et al. 2006).

2.1.3 In vitro conduction analysis

Since each detection electrode of the array is located at a known spatial position, we can easily extract conduction properties within the culture by studying the time delay of action potentials between the different electrodes.

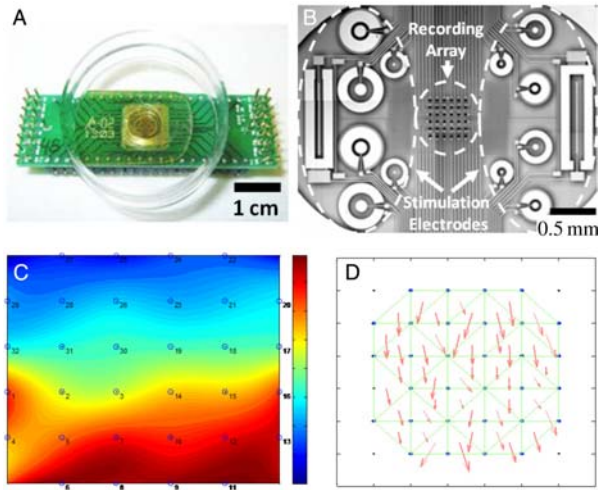


Figure 1. MEA analysis of *in vitro* activation patterns. (A) The array of microelectrodes is wire-bonded to a circuit board carrier. A 35-mm Petri dish with an open centre is adhered to the circuit board using bio-compatible epoxy. (B) A 6×6 array of microelectrodes is fabricated on a glass substrate for electrical recording. The electrical propagation pattern can be represented through lateral isochrone maps or as through velocity vector maps. (C) The lateral isochrones map is an interpolation of the time delay between electrodes, which is displayed by varying shades of colour, overlaid on a representation of the 6×6 electrodes. The depolarisation wave is initiated in the blue region at an activation time = 0 s, and propagates towards the red region, activation time = 0.04 s. (D) The velocity vector map is calculated by grouping the recording electrodes by three, and solving for the direction and magnitude of the time delay.

We characterise the propagation speed and the direction of propagation by recording the electrical signal at all detection electrodes and by analysing the spatio-temporal variation of the recordings. As a characteristic metric for action potential initiation, we introduce the LAT, which we define as the maximum negative slope of the first derivative of the recorded signal.

The propagation of the electrical activity is commonly visualised in two ways, lateral isochrone maps (Lammers et al. 1990) and velocity vector maps (Chen et al. 2010). To create a lateral isochrones map, we first normalise the 6×6 LATs by subtracting the minimum activation time from each recording. Then, we generate the characteristic activation plot, i.e. the 41×41 pixel image of conduction, by performing a cubic spline interpolation between the LATs. To create a lateral isochrones map, we fit the values of the activation plot to a colour-coded contour map. Figure 1(C) displays a representative lateral isochrones map illustrating the initial depolarisation in the blue region and the gradual propagation of the depolarisation wave towards the red region.

To create a velocity vector map, we group the detection electrodes in groups of three. For each electrode triplet, we calculate the magnitude and the direction of

propagation following a method previously described (Bayly et al. 1998). Figure 1(D) shows a representative velocity vector map of the electrical activity within our co-culture system.

2.2 In silico conduction analysis using FEM

To characterise the action potential propagation in a cardiomyocyte–fibroblast co-culture *in silico*, we create a finite element model of the MEA system described in Section 2.1.2. In particular, we utilise the classical FitzHugh–Nagumo equations for electroactive cells (FitzHugh 1961; Nagumo et al. 1962), enhanced by the Aliev–Panfilov modifications (Aliev and Panfilov 1996; Göktepe and Kuhl 2009) for cardiomyocytes.

2.2.1 Mathematical model

Mathematically, we model the excitation of electrically active cells through the action potential ϕ in terms of the flux term, $\text{div } \mathbf{q}$, and the source term, f^ϕ ,

$$\dot{\phi} = \text{div } \mathbf{q}(\phi) + f^\phi(\phi, r). \quad (1)$$

To characterise the global action potential propagation, we use a phenomenological model for the flux vector \mathbf{q} ,

$$\mathbf{q} = \mathbf{D} \cdot \nabla \phi, \quad (2)$$

where $\mathbf{D} = d^{\text{iso}} \mathbf{I} + d^{\text{ani}} \mathbf{n} \otimes \mathbf{n}$ is a second-order diffusion tensor. \mathbf{D} can be either purely isotropic, with $d^{\text{ani}} = 0$, or possess anisotropic contributions, with $d^{\text{ani}} \neq 0$ (Johnston et al. 2008), along pronounced directions \mathbf{n} (Theofilogiannakos et al. 2002). Although the *in vivo* cardiac conduction is highly anisotropic with faster signal propagation along the long axis of the cell, it is common to model randomly oriented *in vitro* systems like ours as macroscopically isotropic. To study the anisotropic conduction *in vitro*, cells are typically cultured on micropatterned cover slips with pre-defined orientation (Rohr et al. 1991), a method that has recently revealed anisotropy ratios of $d^{\text{ani}} : d^{\text{iso}} = 5.6$ (Bursac et al. 2002). To characterise the local action potential profile, we introduce the following source term f^ϕ :

$$f^\phi = c\phi[\phi - \alpha][1 - \phi] - r\phi, \quad (3)$$

which consists of a cubic polynomial in terms of the action potential, $c\phi[\phi - \alpha][1 - \phi]$, and a coupling term introducing the recovery variable r . Here, we choose the scaling parameter to $c = 8.0$ and the oscillation threshold to $\alpha = 0.05$. Although it is common to assume a spatial propagation of the action potential itself, the evolution equation for the recovery variable is usually assumed to be

strictly local.

$$\dot{r} = f^r(\phi, r). \quad (4)$$

It is governed solely through the source term f^r ,

$$f^r = [\gamma + r\bar{\gamma}(\phi)][-r - c\phi[\phi - b - 1]], \quad (5)$$

in terms of parameters $\gamma = 0.002$ and $b = 0.150$ and the additional weighting factor $\gamma + r\bar{\gamma}(\phi)$ with $\bar{\gamma}(\phi) = \mu_1/[\mu_2 + \phi]$. This term allows us to phenomenologically tune the restitution curve through parameters $\mu_1 = 0.02$ and $\mu_2 = 0.03$ (Aliev and Panfilov 1996).

2.2.2 Computational model

Computationally, we discretise the coupled spatio-temporal system of Equations (1) and (4) with finite differences in time and with finite elements in space (Göktepe and Kuhl 2010; Wong et al. 2011). We introduce the action potential ϕ as global degree of freedom at each finite element node, while we evaluate the recovery variable r locally on the integration point level (Göktepe et al. 2010; Kotikanyadanam et al. 2010).

Globally, we transform the nonlinear excitation problem (1) into its residual format $R^\phi = \dot{\phi} - \text{div}(\mathbf{q}) - f^\phi \doteq 0$ in \mathcal{B} , which we complement by the corresponding Dirichlet and Neumann boundary conditions $\phi = \bar{\phi}$ on $\partial\mathcal{B}_\phi$ and $\mathbf{q} \cdot \mathbf{n} = \bar{q}$ on $\partial\mathcal{B}_q$. Here, on the entire boundary $\partial\mathcal{B}$, we assume homogeneous Neumann boundary conditions, $\mathbf{q} \cdot \mathbf{n} = 0$. We obtain the weak form of the residual R^ϕ by an integration over the domain \mathcal{B} , the standard integration by parts and the inclusion of the Neumann boundary conditions. For the spatial discretisation, we discretise the domain of interest \mathcal{B} with n_{el} finite elements \mathcal{B}_e as $\mathcal{B} = \cup_{e=1}^{n_{\text{el}}} \mathcal{B}^e$ and apply the standard isoparametric concept to interpolate the trial and test functions ϕ and $\delta\phi$.

$$\delta\phi = \sum_{i=1}^{n_{\text{en}}} N^i \delta\phi_i, \quad \phi = \sum_{j=1}^{n_{\text{en}}} N^j \phi_j. \quad (6)$$

For the linear quadrilateral elements used in the sequel, N , are the standard bi-linear shape functions and $i, j = 1, \dots, n_{\text{en}}$ are the $n_{\text{en}} = 4$ element nodes. For the temporal discretisation, we partition the time interval of interest \mathcal{T} into n_{stp} subintervals $[t_n, t_{n+1}]$ as $\mathcal{T} = \cup_{n=0}^{n_{\text{stp}}-1} [t_n, t_{n+1}]$ and apply a standard backward Euler time integration scheme in combination with a finite difference approximation of the first-order time derivative $\dot{\phi}$.

$$\dot{\phi} = [\phi - \phi_n]/\Delta t. \quad (7)$$

Here and from now on, we omit the index $(\circ)_{n+1}$ for the sake of brevity and use the common abbreviation $\Delta t :=$

$t - t_n > 0$ for the current time increment. With the discretisations in space (6) and time (7), we can introduce the discrete algorithmic residual,

$$R_I^\phi = \mathbf{A} \int_{\mathcal{B}} N^i \frac{\phi - \phi_n}{\Delta t} + \nabla N^i \cdot \mathbf{q} - N^i f^\phi \, dV \doteq 0, \quad (8)$$

where operator \mathbf{A} symbolises the assembly of all local element residuals at the element nodes i to the global residual at the global nodes I . To solve the discrete system of nonlinear Equations (8), we apply an incremental iterative Newton Raphson solution technique. It is based on the consistent linearisation of the residual $K_{IJ}^\phi = \partial_{\phi J} R_I^\phi$, introducing the global iteration matrix,

$$K_{IJ}^\phi = \mathbf{A} \int_{\mathcal{B}^e} N^i \frac{1}{\Delta t} N^j + \nabla N^i \cdot \mathbf{D} \cdot \nabla N^j - N^i d_\phi f^\phi N^j \, dV, \quad (9)$$

which defines the update of the global vector of unknowns $\phi_I \leftarrow \phi_I - \sum_J K_{IJ}^{\phi-1} R_J^\phi$ at all global nodes I .

Locally, to discretise the recovery variable r in time, we apply a standard finite difference approximation.

$$\dot{r} = [r - r_n]/\Delta t. \quad (10)$$

Using an implicit Euler backward scheme, we rephrase the discrete residual statement of the recovery Equation (4) in the following form:

$$R^r = r - r_n - [[\gamma + r\bar{\gamma}][-r - c\phi[\phi - b - 1]]]\Delta t \doteq 0. \quad (11)$$

Its consistent linearisation $K^r = \partial_r R^r$ with

$$K^r = 1 + [\gamma + \bar{\gamma}[2r + c\phi[\phi - b - 1]]]\Delta t \quad (12)$$

defines the iteration scheme for the incremental update of the recovery variable $r \leftarrow r - K^{r-1} R^r$ on the integration point level. At local equilibrium, we compute the source term for $f^\phi = c\phi[\phi - \alpha][1 - \phi] - r\phi$, the global residual of the excitation problem (8) and its linearisation $d_\phi f^\phi = \partial_\phi f^\phi + \partial_r f^\phi d_\phi r$ for the global Newton iteration (9).

2.2.3 In silico conduction analysis

Motivated by the *in vitro* model of Section 2.1.3, we create an *in silico* finite element model of the co-culture system of cardiomyocytes and fibroblasts. We represent the culture system through a 2D flat sheet discretised with 1225 bi-linear finite elements of $20 \mu\text{m} \times 20 \mu\text{m}$ each, covering a total area of $700 \times 700 \mu\text{m}^2$. We model cardiomyocytes as electrically active and conductive as described in Sections 2.2.1 and 2.2.2. For the sake of simplicity, we model fibroblasts as non-conductive,

keeping in mind that, in reality, they might be actively engaged in the conduction system, however, at a much lower inherent conductivity than cardiomyocytes (Xie et al. 2009). To identify the effect of cell morphology on signal propagation, we conduct two sets of simulations. For the first set, labelled as 1:1 aspect ratio, we assume that cardiacmyocytes and fibroblasts are of equal size. For the second set, labelled as a 1:2 aspect ratio, we assume that fibroblasts are twice as long as cardiomyocytes.

To establish quantitative purity–conduction relationships, we create 21 different co-culture models with a cardiomyocyte-to-fibroblast ratio varying from 100:0 to 0:100 in increments of 5. For each cardiomyocyte-to-fibroblast ratio, we analyse $n = 5$ realisations. Similar to a technique reported in the literature (Zlochiver et al. 2008), for each realisation, we assign each of the 1225 elements a randomly selected cell type, either cardiomyocyte or fibroblast.

To initiate signal propagation throughout the culture system, we select one random cardiomyocyte within the culture and stimulate it with an external electrical signal. In analogy to the *in vitro* set-up, we record the electrical signal at 6×6 virtual recording sites spaced 100 μm apart, covering an area of $500 \times 500 \mu\text{m}^2$ located in the centre of our sample. Similar to the *in vitro* conduction analysis described in Section 2.1.3, we then generate the characteristic activation plot, i.e. the 41×41 pixel image of conduction, by performing a cubic spline interpolation between the virtually recorded 6×6 LATs.

2.3 Co-occurrence matrix

In Section 2.1.3, we have illustrated how to extract lateral isochrone maps and velocity vector maps from our MEA recordings. Although both mappings provide insight into the qualitative nature of the overall conduction pattern, neither of them is capable to characterise disturbed conduction in heterogeneous co-culture systems through quickly accessible scalar-valued metrics. Here, we suggest a novel evaluation technique, co-occurrence analysis, to quantify the uniformity and homogeneity of an electrical conduction pattern (Haralick 1979). Originally designed for feature recognition in texture analysis (Julesz 1962), the co-occurrence analysis can be adapted to post-process activation plots obtained from MEA recordings or FEM simulations.

In our case, the underlying activation plot consists of 41×41 discrete values, generated from an interpolation of the *in vitro* and *in silico* recorded 6×6 LATs. By its definition, the corresponding co-occurrence matrix

$$C_{ij} = \sum_{r=1}^n \sum_{s=1}^m \begin{cases} 1, & \text{if } I_{rs} = i \text{ and } I_{r+1,s+1} = j, \\ 0, & \text{otherwise} \end{cases} \quad (13)$$

is a correlation matrix, which quantifies how often two neighbouring entries occur in the $n \times m$ activation plot I_{rs} , one with a LAT of i , the other one with a LAT of j . For example, the co-occurrence matrix component $C_{i=2,j=1} = 8$ indicates that a LAT of $i = 2$ is found next to a LAT of $j = 1$, a total of eight times in the discrete activation plot.

Since the co-occurrence matrix is a transform based on LATs, its dimension $i \times j$ depends on the number of different activation times found within the activation plot. When constructing the co-occurrence matrix, we can define its sensitivity based on the distance between pairs of LATs (Haralick 1979). In Equation (13), we have chosen a distance of ± 1 to capture all pairs of nearest neighbours as illustrated in Figure 2. Since LAT pairs do not account for directionality, the co-occurrence matrix is always square and always symmetric, $C_{ij} = C_{ji}$. In addition, the total number of co-occurrence pairs within activation plots of the same size is equivalent, here it is always 41×41 . We therefore normalise the co-occurrence matrix by dividing each entry by the total number of occurrence pairs, here 1681, thus making the co-occurrence matrix a collection of probabilities of occurrences. Throughout this manuscript, we use Matlab (The Mathworks, Natick, MA) to calculate the co-occurrence matrices for the *in vitro*- and *in silico*-generated activation plots from Sections 2.1.3 and 2.2.3, respectively. The underlying algorithm is illustrated in Figure 2.

Figure 3 displays representative activation plots and the corresponding co-occurrence matrices of five characteristic examples: linear gradient, sine wave, criss cross pattern, spiral wave and random noise, from left to right.

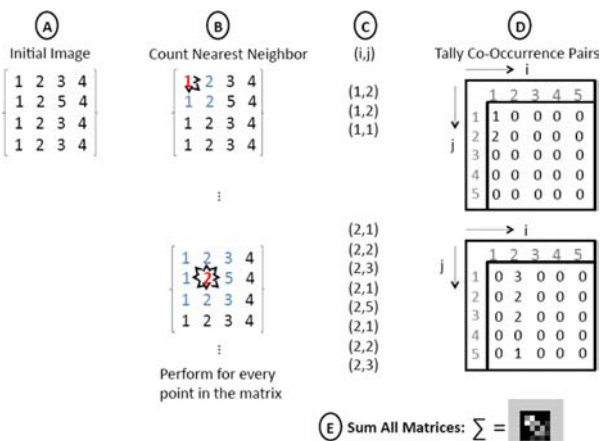


Figure 2. Algorithm to calculate the co-occurrence matrix based on counting the number of incidents that each LAT occurs in an activation plot (A), each entry is paired with its nearest neighbourer (B) and noted (C). The values within each pair correspond to the coordinates of the co-occurrence matrix, and the number of occurrences is tallied (D). Steps (B)–(D) are repeated for each entry in the original matrix in (A) such that the final co-occurrence matrix is the sum of all these matrices.

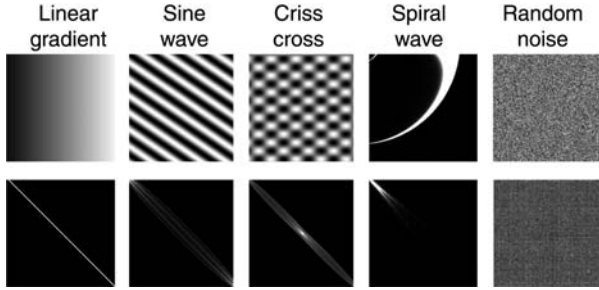


Figure 3. Examples of characteristic activation plots (top) and their co-occurrence matrices (bottom). Activation plots consist of 300×300 pixels and exhibit greyscale intensities from 0 to 255. Smooth images are characterised through co-occurrence matrices that are clustered around the diagonal (left). The more the image is disordered, the farther away from the diagonal the co-occurrence matrix is populated (right).

It is important to remember that the population of the co-occurrence matrix is not representative of the geometric excitation pattern itself. Rather, it represents the local distribution of pixel pairs. Uniform conduction patterns, e.g. the linear gradient pattern, exhibit an activation plot that changes steadily as the depolarisation wave propagates. This level of regularity creates a co-occurrence matrix with values heavily concentrated along the diagonal. Non-uniform conduction patterns, e.g. the spiral wave pattern, exhibit large greyscale differences between neighbouring nodes, yielding a co-occurrence matrix with values farther away from the diagonal. The co-occurrence matrix can further indicate whether the depolarisation wave is evenly propagated. A disproportionate number of early activation times results in a cluster of occurrences in the upper left corner, e.g. for the spiral wave pattern, whereas a disproportionate number of late activation times results in a cluster of occurrences in the lower right corner. The co-occurrence matrix is therefore a measure of uniformity and homogeneity.

2.4 Co-occurrence energy and contrast

Two characteristic features of the co-occurrence matrix, co-occurrence energy and co-occurrence contrast, are capable to quickly portray the status of a depolarisation wave (Haralick et al. 1973; Zucker and Terzopoulos 1980). The energy of a co-occurrence matrix, which is sometimes also referred to as the angular second moment,

$$\text{energy} = \sum_{i=1}^n \sum_{j=1}^m C_{ij}^2, \quad (14)$$

is the sum of the squares of each matrix entry, here evaluated for an $n \times m$ co-occurrence matrix C_{ij} . In our case, $n = m$ is the number of different activation times

Table 1. Examples of characteristic activation plots from Figure 3 and their corresponding co-occurrence energy and contrast.

	Linear gradient	Sine wave	Criss cross	Spiral wave	Random noise
Energy	893.5	2978.1	595.9	134210	8.6
Contrast	0.5	155.5	780.4	240.3	7806.8

Notes: The energy is highest for images with sharp fronts like the spiral wave and lowest for uniform images like the random noise. The contrast is highest for images with large spatial variations like the random noise and lowest for homogeneous images like the linear gradient.

found within the activation plot. The co-occurrence energy is a measure for the *uniformity* of the co-occurrence matrix (Davis et al. 1979). Accordingly, it is lowest when all entries are equal. Although the energy is a useful metric to access whether there are many particular occurrences, it fails to quantify whether values are clustered along the diagonal or not. The contrast of a co-occurrence matrix,

$$\text{contrast} = \sum_{i=1}^n \sum_{j=1}^m [i - j]^2 C_{ij}, \quad (15)$$

is a metric that characterises whether a large proportion of co-occurrence pairs is located along the diagonal. This is achieved by assigning a larger weight, $[i - j]^2$, to entries farther away from the diagonal. The co-occurrence contrast is a measure for the *homogeneity* of the spatial distribution of local features (Davis et al. 1979). Accordingly, larger contrast values indicate a more heterogeneous conduction.

Table 1 illustrates the co-occurrence energy and contrast for the characteristic activation plots shown in Figure 3. The energy is highest for images with sharp fronts like the spiral wave. It is lowest for uniform images like the random noise. The contrast is highest for images with large spatial variations like the random noise. It is lowest for homogeneous images like the linear gradient. In the following section, we illustrate the potential of the co-occurrence matrix and its energy and contrast to quantify conduction patterns of heterogeneous cardiomyocyte–fibroblast co-cultures for both the *in vitro* and the *in silico* co-culture models created in Sections 2.1 and 2.2.

3. Results

3.1 In vitro conduction analysis using MEAs

Figure 4 shows a representative set of micrographs for varying cardiomyocyte-to-fibroblast ratios, here illustrated for 0:100, 60:40, 70:30, 80:20, 90:10 and 100:0. Cardiomyocytes and fibroblasts can be clearly distinguished by their characteristic morphologies. Although murine HL-1 cardiomyocytes, dominant towards the lower

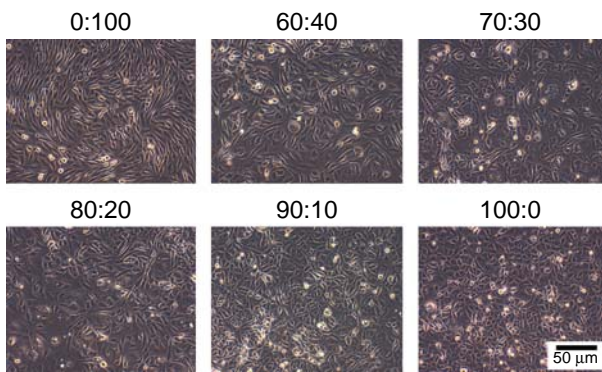


Figure 4. Optical micrographs of *in vitro* co-cultured murine HL-1 cardiomyocytes and murine 3T3 fibroblasts. We systematically increase the cardiomyocyte-to-fibroblast ratio from 0:100 to 100:0 in increments of 5. As the cardiomyocyte-to-fibroblast ratio increases, here shown for 0:100, 60:40, 70:30, 80:20, 90:10 and 100:0, the co-culture system becomes increasingly dominated by circle-shaped cardiomyocytes (bottom right) and less dominated by spindle-shaped fibroblasts (top left).

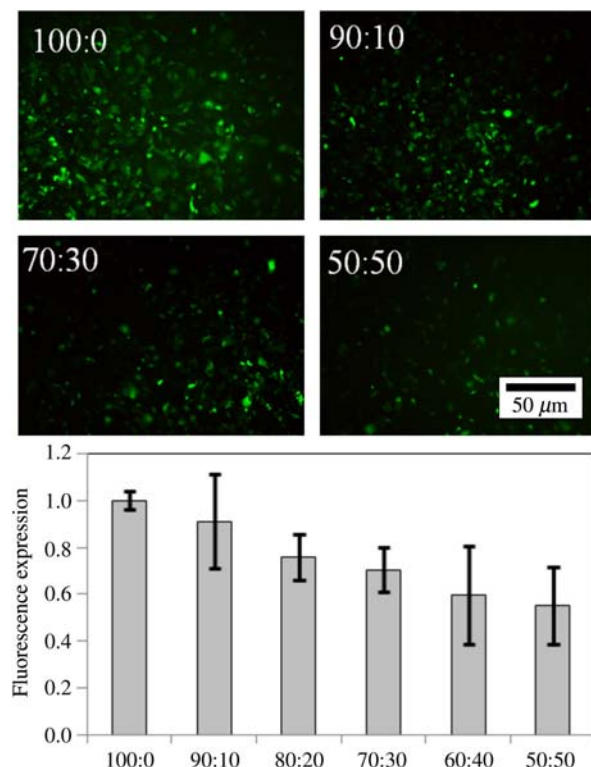


Figure 5. Fluorescence expression of *in vitro* co-cultured murine HL-1 cardiomyocytes and murine 3T3 fibroblasts, where HL-1 cardiomyocytes are transfected with GFP through a lentiviral vector. We systematically decrease the cardiomyocyte-to-fibroblast ratio from 100:0 to 0:100 in increments of 5. Qualitatively, GFP expression decreases with decreasing cardiomyocyte-to-fibroblast ratio, here shown for 100:0, 90:10, 70:30 and 50:50 (top). Quantitatively, GFP expression decreases approximately linearly with decreasing cardiomyocyte-to-fibroblast ratios, shown in terms of averages and standard deviations for groups of $n = 3$ (bottom).

right corner, take a more spherical shape, murine 3T3 fibroblasts, dominant towards the upper left corner, are characterised through a spindle-type morphology.

Figure 5 documents the fluorescence expression of co-cultures of murine HL-1 cardiomyocytes and murine 3T3 fibroblasts, where HL-1 cardiomyocytes are transfected with a GFP marker through a lentiviral vector. Qualitatively, fluorescent imaging with 450 nm excitation and 515 nm emission wavelengths reveals decreased GFP expression with decreasing cardiomyocyte-to-fibroblast ratios, here illustrated for ratios of 100:0, 90:10, 70:30 and 50:50.

Although the pure population of cardiomyocytes is confluent, GFP expression is not ubiquitous throughout the culture of transfected cells. We therefore normalise the fluorescence intensity with respect to the pure cardiomyocyte population displayed in the upper left corner. Quantitatively, GFP expression decreases approximately linearly with decreasing cardiomyocyte-to-fibroblast ratios, shown in terms of averages and standard deviations for groups of $n = 3$, in the bottom graph of Figure 5.

Figure 6 summarises the action potential profiles for co-cultures of different cardiomyocyte-to-fibroblast ratios for all 32 electrodes on the MEAs. When decreasing the cardiomyocyte-to-fibroblast ratio, here shown for 100:0, 80:20, 70:30 and 50:50, the smoothness of the conduction pattern clearly decreases. While the 100:0 plain cardiomyocyte culture, shown on the left, displays a homogeneous conduction pattern, the 80:20 and 70:30 co-cultures, shown in the middle, demonstrate an intermediate behaviour between smooth conduction and isolated spontaneous beating. The 50:50 co-culture, shown on the right, displays spontaneous beating, indicated through isolated signals in specific channels, with no sign of homogenous conduction.

Figure 7 shows two representative velocity vector maps and the per cent active area for co-cultures of murine HL-1 cardiomyocytes and murine 3T3 fibroblasts. Although pure 100:0 cultures of cardiomyocytes, shown on the left, support continuous almost unidirectional propagation throughout the system, heterogeneous 80:20 populations, shown on the right, exhibit a non-smooth conduction pattern impeded by non-conductive fibroblasts.

By systematically decreasing the cardiomyocyte-to-fibroblast ratio in increments of 5, and exploring $n = 3$ groups for each ratio, we identify the 50:50 ratio to be as the lowest threshold necessary to ensure signal detection, as demonstrated in the bottom graph of Figure 7. In two out of three MEAs plated with this ratio, we record action potentials in only two channels, whereas the third MEA in the group does not display any action potentials at all. Recorded beats are asynchronous between the different channels. This indicates that the 50:50 ratio, although sufficient for islets of activity of about 1 mm^2 each, does not contain enough cardiomyocytes to support continuous conduction throughout the entire sample.

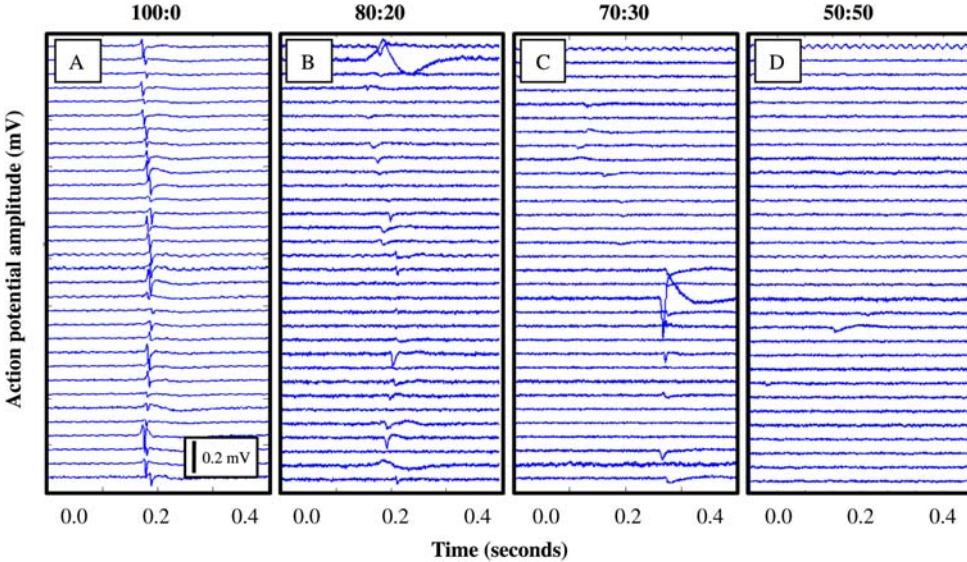


Figure 6. Action potential profiles of *in vitro* co-cultured murine HL-1 cardiomyocytes and murine 3T3 fibroblasts, displayed for all 32 electrodes on the MEA. We systematically decrease the cardiomyocyte-to-fibroblast ratio from 100:0 to 0:100 in increments of 5. The smoothness of the conduction pattern decreases with decreasing cardiomyocyte-to-fibroblast ratio, here shown for 100:0, 80:20, 70:30 and 50:50. The 100:0 plain cardiomyocyte culture displays a homogeneous conduction pattern (left). The 80:20 and 70:30 co-cultures demonstrate an intermediate behaviour between smooth conduction and isolated spontaneous beating (middle). The 50:50 co-culture displays spontaneous beating, indicated through isolated signals in specific channels, with no sign of homogenous conduction (right).

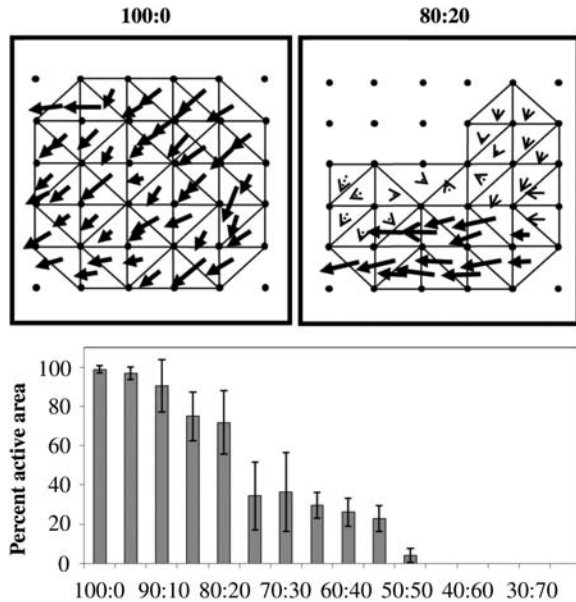


Figure 7. Velocity vector maps (top) and per cent active area (bottom) of *in vitro* co-cultured murine HL-1 cardiomyocytes and murine 3T3 fibroblasts. We systematically decrease the cardiomyocyte-to-fibroblast ratio from 100:0 to 0:100 in increments of 5. The active area fraction decreases with decreasing cardiomyocyte-to-fibroblast ratio, as the electrical activity becomes less synchronised. Pure 100:0 cultures of cardiomyocytes (left) support continuous, almost unidirectional, propagation throughout the homogeneous population. Heterogeneous 80:20 populations (right) exhibit a non-smooth conduction pattern impeded by non-conductive fibroblasts. The active area fraction (bottom) reveals that action potentials can only be recorded above a critical 50:50 ratio threshold.

Beginning with a 70:30 cardiomyocyte-to-fibroblast ratio, samples display similar asynchronous patterns of spontaneous beating between 12 ± 2 channels. Activation patterns typically group into two beating patches of approximately 6 mm^2 each. One of the 80:20 ratios demonstrates a small depolarisation wavefront throughout the heterogeneous population, with one large synchronously beating patch that averages 20 ± 3 active electrodes, approximately corresponding to an area of 20 mm^2 .

3.2 In silico conduction analysis using FEM

Figure 8 illustrates the lateral isochrone maps simulated for cardiomyocyte-to-fibroblast ratios of 100:0, 90:10, 70:30, 50:50, 30:70 and 10:90 using our finite element model. Similar to the lateral isochrones map in Figure 1(C), early stage depolarisation is shown in blue, whereas late depolarisation is shown in red.

When systematically decreasing the cardiomyocyte-to-fibroblast ratio from 100:0 to 0:100 in increments of 5, and evaluating $n = 5$ realisations of statistically random cell distributions for each set, we observe that continuous electrical conduction paths do not form below a critical cardiomyocyte-to-fibroblast threshold of 50:50. The top row of Figure 8 shows the results for the 1:1 aspect ratio simulation, for which cardiomyocytes and fibroblasts are of equal size. The bottom row illustrates the results for the 1:2 aspect ratio simulation, for which fibroblasts are

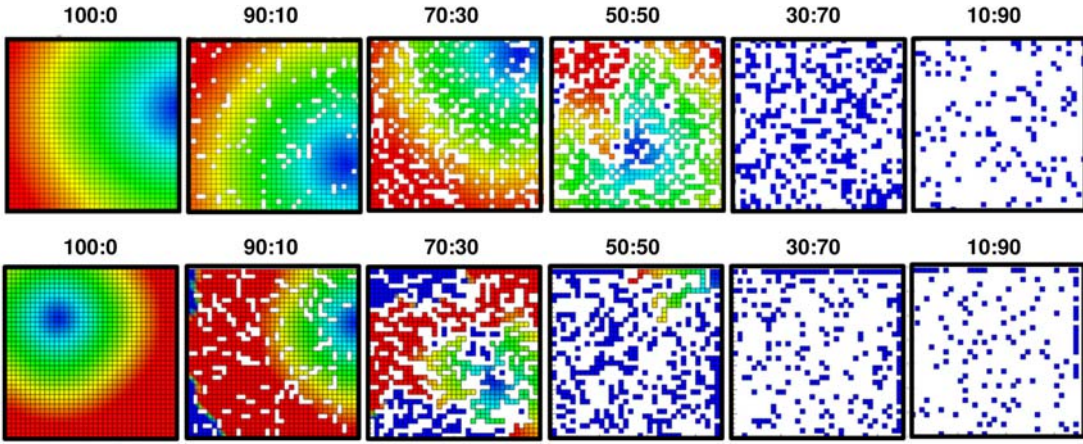


Figure 8. Lateral isochrones map of *in silico* co-cultured electrically active, conductive cardiomyocytes and non-conductive fibroblasts, simulated with our finite element model. We systematically decrease the cardiomyocyte-to-fibroblast ratio from 100:0 to 0:100 in increments of 5, here shown for 100:0, 90:10, 70:30, 50:50, 30:70 and 10:90. For the first set of simulations, 1:1 aspect ratio (top row), we model cardiomyocytes and fibroblasts to be of equal size. For the second set of simulations, 1:2 aspect ratio (bottom row), we model fibroblasts twice as long as cardiomyocytes. Continuous electrical conduction paths do not form below a critical cardiomyocyte-to-fibroblast threshold of 50:50. Similar to the lateral isochrones map in Figure 1(C), early stage depolarisation is shown in blue, while late depolarisation is shown in red.

twice as long as cardiomyocytes. The conduction pattern is slightly smoother for the equal aspect ratio, which is particularly apparent close to the critical threshold ratio of 50:50.

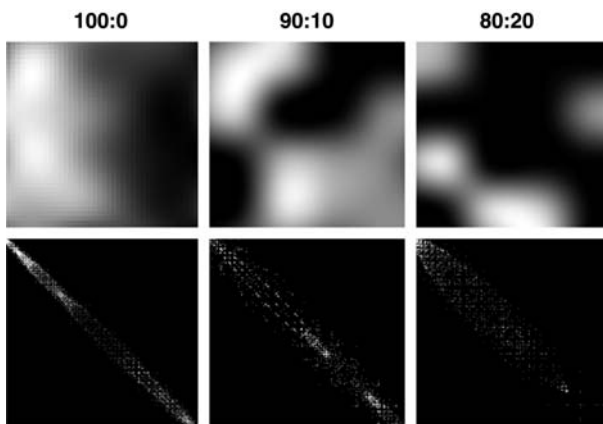


Figure 9. Isolated activation plots (top) and co-occurrence matrices (bottom) of *in vitro* co-cultured murine HL-1 cardiomyocytes and murine 3T3 fibroblasts. We systematically decrease the cardiomyocyte-to-fibroblast ratio from 100:0 to 0:100 in increments of 5. Representative activation plots display the LATs as a depolarisation wave travels from the white regions to the dark regions. Pure 100:0 cardiomyocyte cultures (left) support gradual, smooth activation patterns indicated through a single unique propagation front. More heterogeneous 90:10 (middle) and 80:20 (right) populations exhibit non-smooth activation patterns resulting in a more diffuse signal propagation. With decreasing cardiomyocyte-to-fibroblast ratios, the co-occurrence matrices become less focused along their diagonals and more populated in off-diagonal regions.

3.3 Co-occurrence matrix

Figure 9 illustrates representative activation plots, which indicate the LATs as a depolarisation wave travels from the white regions to the dark regions.

While pure cultures of cardiomyocytes, shown on the left, support gradual smooth activation patterns, heterogeneous co-cultures, shown in the middle and on the right, exhibit non-smooth activation patterns, resulting in a more diffuse signal propagation. The bottom row of Figure 9 documents the corresponding co-occurrence matrices. With decreasing cardiomyocyte-to-fibroblast ratios, shown from left to right, the co-occurrence matrices become less focused along their diagonals and more populated in off-diagonal entries. This population of the co-occurrence matrices agrees nicely with the examples of characteristic co-occurrence matrices documented in Figure 3.

3.4 Co-occurrence energy and contrast

Figure 10 displays the co-occurrence energy and contrast for co-cultures of murine HL-1 cardiomyocytes and murine 3T3 fibroblasts. For systems with a cardiomyocyte-to-fibroblast ratio of less than 80:20, we observe that less than half of the electrodes of the MEA record an electrical signal.

Analyses of samples below this threshold are rather based on interpolated values than on actual data and are therefore not included in the co-occurrence analysis. Accordingly, in Figure 10, we only show results above this critical threshold of 80:20. We display energy and contrast values for each co-culture group in terms of averages and standard deviations for groups of $n = 3$, normalised to the

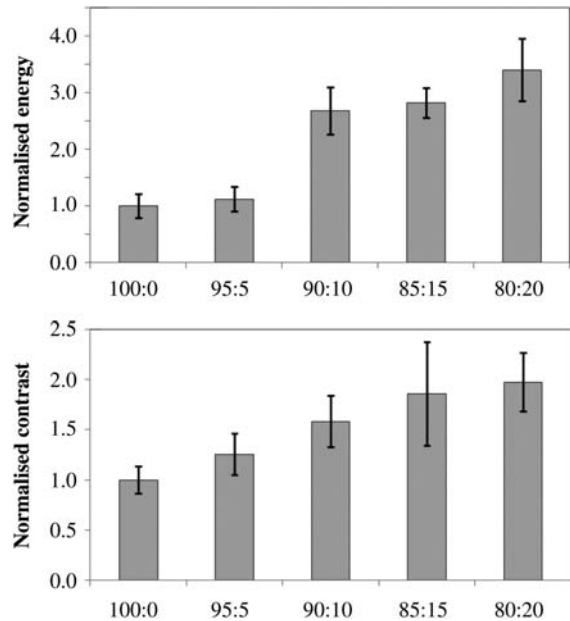


Figure 10. Co-occurrence energy (top) and co-occurrence contrast (bottom) of *in vitro* co-cultured murine HL-1 cardiomyocytes and murine 3T3 fibroblasts. We systematically decrease the cardiomyocyte-to-fibroblast ratio from 100:0 to 0:100 in increments of 5. We exclude results below the critical cardiomyocyte-to-fibroblast threshold of 80:20, for which less than half of the microelectrodes record an electrical signal. Energy and contrast values for each co-culture group are displayed in terms of averages and standard deviations for groups of $n = 3$, normalised to the average value of the 100:0 group. Both co-occurrence energy and contrast increase with decreasing cardiomyocyte-to-fibroblast ratios, indicating the gradual disruption of the electrical conduction system.

average value of the 100:0 group. Both co-occurrence energy and contrast increase with decreasing cardiomyocyte-to-fibroblast ratios, indicating a severely disrupted electrical conduction system. Figure 10 demonstrates an increase in energy and contrast with a decreasing cardiomyocyte-to-fibroblast ratio. Since the energy is the sum of squared values of the whole co-occurrence matrix, it increases considerably in the presence of a large number of a particular pair of LATs. In this case, areas on the array that do not exhibit electrical activity result in activation plots with regions that are all the same value. A high-energy value therefore indicates inconsistencies in a co-culture, here caused by the lack of conduction. The contrast increases steadily as the cardiomyocyte-to-fibroblast ratio decreases, but not as drastically as the energy. Quantifying the deviation from the diagonal of a co-occurrence matrix, large contrast values indicate increased disruption of conduction.

Figure 11 illustrates the co-occurrence energy and contrast extracted from our finite element simulations. Both co-occurrence energy and contrast increase with decreasing cardiomyocyte-to-fibroblast ratios, indicating a

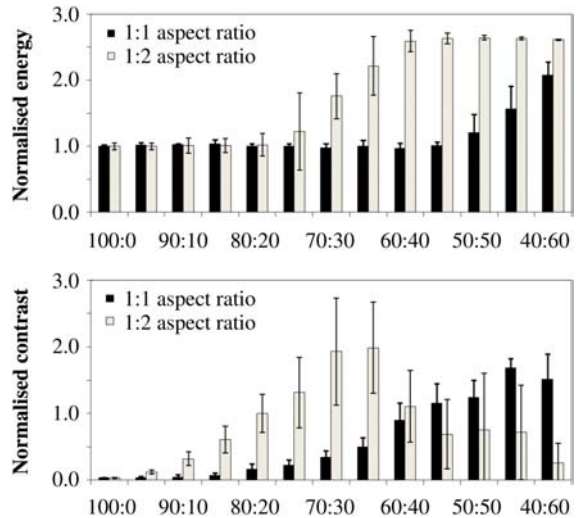


Figure 11. Co-occurrence energy (top) and co-occurrence contrast (bottom) of *in silico* co-cultured electrically active, conductive cardiomyocytes and non-conductive fibroblasts, simulated with our finite element model. We systematically decrease the cardiomyocyte-to-fibroblast ratio from 100:0 to 0:100 in increments of 5. Energy and contrast values for each co-culture group are displayed in terms of averages and standard deviations for groups of $n = 5$, normalised to the average value of the 100:0 group. Both co-occurrence energy and contrast increase with decreasing cardiomyocyte-to-fibroblast ratios, indicating the gradual disruption of the electrical conduction system.

severely disrupted electrical conduction system. Simulations based on the square fibroblast model, 1:1 aspect ratio, do not exhibit a significant change in energy from the pure cardiomyocyte population down to a cardiomyocyte-to-fibroblast ratio of 45:55, whereas simulations based on the rectangular fibroblast model, 1:2 aspect ratio, exhibit this change at the 75:25 ratio. Significant changes in contrast begin at the 80:20 ratio for the square fibroblast model, whereas they already begin at the 95:5 ratio for rectangular fibroblast model. As the relative number of fibroblasts increases, the energy begins to increase due to large patches of non-conductive regions, which lead to large quantities of similar co-occurrence pairs. With increasing number of co-occurrence pairs, fewer variations are observed, which lead to the decrease in contrast. For square fibroblasts, this decrease takes place at ratios of 40:60; for rectangular fibroblasts, it takes places slightly earlier, at ratios of 60:40.

4. Discussion

In this study, we establish an easily reproducible method to generate purity–conduction relationships for co-culture systems with different volume fractions. To characterise conduction patterns *in vitro*, we utilise a custom-designed MEA platform to analyse conduction in co-cultured

murine HL-1 cardiomyocytes and murine 3T3 fibroblasts. For our 2D culture system, we observe that fibroblast concentrations $>10\%$ severely disrupt the electrical conduction as shown in the bottom graph of Figure 7. The increase in co-occurrence energy reported in Figure 10, top, which indicates a loss of uniformity, is in excellent agreement with this observation. The increase in co-occurrence contrast reported in Figure 10, bottom, which indicates a loss of homogeneity, is in general agreement with these findings; yet the contrast increases more gradually and almost linearly. The population of the co-occurrence matrix shown in Figure 9 reveals that heterogeneous samples exhibit co-occurrence matrices that are not evenly populated along the diagonal. This implies that there is an uneven distribution of time delays between the individual electrodes. This breakdown of smooth conduction is already visible for cardiomyocyte-to-fibroblast ratios of 90:10, illustrated in Figure 9, middle, and in Figure 10. Although local electrical signals can be recorded at relatively low cardiomyocyte-to-fibroblast ratios, the global conduction pattern is extremely sensitive to the presence of small number of fibroblasts. This observation is in good qualitative agreement with findings reported in the literature (Miragoli et al. 2006). Since this study is meant as a first proof-of-principle, we accept the inherent limitation that we only acquire signals at 6×6 recording sites, from which we interpolate a discrete 41×41 activation plot for the co-occurrence analysis. However, it remains to be shown, how the purity-conduction relationships of our 2D model system scale up to three dimensions (Kohl et al. 2005). We anticipate that trends will be similar, whereas the critical threshold ratio to maintain smooth conduction might be lower in the 3D *in vivo* setting (Kehat et al. 2004).

To characterise conduction patterns *in silico*, we use finite element models of co-cultured electrically active, conductive cardiomyocytes and non-conductive fibroblasts. Although we could potentially record our electrical signal at a much higher spatial resolution, we mimic the *in vitro* analysis and establish 6×6 virtual recording sites, from which we interpolate the discrete 41×41 activation plot. Qualitatively, the observed trends of the FEM-based *in silico* conduction analysis displayed in Figure 8 correlate well with the MEA-based *in vitro* conduction analysis shown in Figure 9. Quantitatively, the first set of computations, shown in the top row of Figure 8, predicts a lower critical threshold to maintain smooth conduction using equal-sized cells. Compared with the critical 80:20 ratio from the *in vitro* conduction analysis, the first *in silico* analysis remains conductive well past the 50:50 ratio. We hypothesise that the equal cell size model is overly simplistic because it does not capture the morphological differences between spindle-shaped 3T3 fibroblasts and round HL-1 cardiomyocytes. Accordingly, we refine the computational model and perform a second

set of simulations now using elongated fibroblasts shown in the bottom row of Figure 8. With this morphological refinement, the critical thresholds to maintain conduction increase to approximately 80:20 as illustrated in Figure 11, and agree nicely with the *in vitro* model. Despite these promising preliminary results, our computational model has two major limitations. First, we model fibroblasts as non-conductive, although experimental studies suggest that fibroblasts might play a more important role in cardiac electrophysiology than simply acting as passive electrical insulators (Rook et al. 1992; Gadesius et al. 2003). To further elaborate this issue, we are currently analysing the impact of slightly conducting fibroblasts in analogy to a recently proposed finite difference-based conductivity analysis (Zlochiver et al. 2008). Second, for the sake of simplicity, we have applied a pure mono-domain formulation for the co-culture system (Göktepe and Kuhl 2009). We have recently developed a bi-domain formulation for cardiac tissue (Dal et al. 2011), which we will utilise in the future to better adjust the computational readouts to the electrical recordings (Sundnes et al. 2002).

Co-occurrence analysis allows us to quantify and compare our *in vitro* and *in silico* created conduction patterns. Co-occurrence energy and contrast are known to quickly monitor uniformity and homogeneity of a texture (Haralick 1979). Both features display significant differences between smooth conduction, i.e. in cultures with 100:0 and 95:5 cardiomyocyte-to-fibroblast ratios, and disrupted conduction, i.e. in cultures with lower cardiomyocyte ratios. Co-occurrence analysis has significant relevance towards understanding the arrhythmogenic risk of stem cell transplantation in the heart. This procedure remains controversial because the mechanisms behind the electrical integration of transplanted cells into the host system remain unclear (Kehat et al. 2004). Even the type of graft cells to transplant is still under considerable debate. In addition to using cells from a cardiac lineage, there is evidence that cells outside this lineage, such as mesenchymal stem cells (Marthur and Martin 2004) or skeletal myoblasts (Menasche et al. 2003), may support cardiac tissue regeneration. The complexity of live models has made it difficult to truly understand how host tissue reacts electrically to transplanted cells. Therefore, further work is necessary to probe how the electrical environment affects stem cell integration. Until electrical integration takes place, transplanted cells may not play any functional role (Abilez, Baugh et al. 2011).

5. Conclusion

Various cardiac diseases and treatment options change the local volume fraction of conducting cells. This may alter existing conduction pathways and may increase the risk of arrhythmias. Co-culture systems are illustrative model

systems to systematically investigate the mismatch in conductivity of different cell types and its impact on arrhythmogenesis. From MEA recordings, disturbances in conduction are easily detectable with the human eye; however, there is no automated method to quantify conduction patterns algorithmically in terms of easily accessible characteristic metrics. Here, we demonstrate that co-occurrence analysis, a method that was originally developed for feature recognition in texture analysis, can quickly portray the status of an excitation wave, and can provide insightful information about conduction disturbances. To illustrate the potential of this technique, we calculate co-occurrence matrices, energy and contrast using experimentally and computationally created conduction patterns of different cardiomyocyte–fibroblast cocultures. We show that the population of the co-occurrence matrix is correlated with the smoothness of signal propagation. By systematically reducing the cardiomyocyte-to-fibroblast ratio, we demonstrate that co-occurrence energy is a measure for pattern uniformity, while co-occurrence contrast is an indicator for pattern homogeneity. Overall, co-occurrence analysis is an easily reproducible method to create purity–conduction relationships for co-culture systems with different volume fractions. In particular, in view of stem cell therapies, we expect co-occurrence analysis to provide valuable quantitative insight into the integration of foreign cells into a functional host system.

Acknowledgements

We would like to thank Shilpi Roy for her help in establishing cell culture protocols and Dr Jeff Rogers for his intellectual insight into the establishment of the co-occurrence matrix. This work was supported in part by the NSF Graduate Student Research Fellowship (MQC), by the Sang Samuel Wang Stanford Graduate Fellowship (JW), by the NSF CAREER Award CMMI-0952021(EK) and by the California Institute for Regenerative Medicine through cooperative agreement RS1-00232-1 (GTAK).

References

- Abilez OJ, Baugh JA, Gorrepati ML, Prakash R, Lee-Messer C, Huang M, Jia F, Yu J, Wilson KD, Wu JC et al. 2011. Optogenetic control of human heart cells. submitted for publication.
- Abilez OJ, Wong J, Prakash R, Deisseroth K, Zarins CK, Kuhl E. 2011. Multiscale computational models for optogenetic control of cardiac function. *Biophys J.* 101: 1326–1334.
- Aliev RR, Panfilov AV. 1996. A simple two-variable model of cardiac excitation. *Chaos Soliton Fract.* 7:293–301.
- American Heart Association. 2010. Heart disease and stroke statistics – 2010 update. Dallas: American Heart Association.
- Bayly PV, KenKnight BH, Rogers JM, Hillsley RE, Ideker RE, Smith WM. 1998. Estimation of conduction velocity vector fields from epicardial mapping data. *IEEE Trans Biomed Eng.* 45:563–571.
- Bursac N, Parker KK, Iravanian S, Tung L. 2002. Cardiomyocyte cultures with controlled macroscopic anisotropy – a model for functional electrophysiological studies of cardiac muscle. *Circ Res.* 91:E45–E54.
- Camelliti P, McCulloch AD, Kohl P. 2005. Microstructured cocultures of cardiac myocytes and fibroblasts: a two-dimensional *in vitro* model of cardiac tissue. *Microsc Microanal.* 11:249–259.
- Cao F, Lin S, Xie X, Ray P, Patel M, Zhang X, Drukier M, Dylla S, Connolly AJ, Chen X et al., 2006. *In-vivo* visualization of embryonic stem cell survival, proliferation, and migration after cardiac delivery. *Circulation.* 113:1005–1014.
- Chang MG, Tung L, Sekar RB, Chang CY, Cysyk J, Dong P, Marban E, Abraham R. 2006. Proarrhythmic potential of mesenchymal stem cell transplantation revealed in an *in vitro* coculture model. *Circulation.* 113:1832–1842.
- Chen MQ, Whittington RH, Day PW, Kobilka BR, Giovangrandi L, Kovacs GTA. 2010. A device for separated and reversible co-culture of cardiomyocytes. *Biotech Prog.* 26:1164–1171.
- Claycomb WC, Nicholas J, Lanson A, Stallworth BS, Egeland DB, Delcarpio JB, Bahinski A, Nickolas J, Izzo J. 1998. HL-1 cells: a cardiac muscle cell line that contracts and retains phenotype characteristics of the adult cardiomyocyte. *Proc Natl Acad Sci.* 95:2979–2984.
- Dal H, Göktepe S, Kaliske M, Kuhl E. 2011. A fully implicit finite element method for bidomain models of cardiac electrophysiology. *Comput Meth Biomed Eng.* in press. doi:10.1080/10255842.2011.554410.
- Davis LS, Johns SA, Aggarwal JK. 1979. Texture analysis using generalized co-occurrence matrices. *IEEE Trans Pattern Anal Mach Intell.* 1:251–259.
- FitzHugh R. 1961. Impulses and physiological states in theoretical models of nerve membranes. *Biophysical J.* 1:445–466.
- Gaudesius G, Miragoli M, Thomas SP, Rohr S. 2003. Coupling of cardiac electrical activity over extended distances by fibroblasts of cardiac origin. *Circ Res.* 93:421–428.
- Gilchrist KH, Barker VN, Fletcher LE, DeBusschere BD, Ghanouni P, Giovangrandi L, Kovacs GTA. 2001. General purpose, field portable cell-based biosensor platform. *Biosens Bioelectron.* 16:557–564.
- Göktepe S, Kuhl E. 2009. Computational modeling of cardiac electrophysiology: a novel finite element approach. *Int J Numer Meth Eng.* 79:156–178.
- Göktepe S, Kuhl E. 2010. Electromechanics of the heart: a unified approach to the strongly coupled excitation-contraction problem. *Comput Mech.* 45:227–243.
- Göktepe S, Wong J, Kuhl E. 2010. Atrial and ventricular fibrillation: computational simulation of spiral waves in cardiac tissue. *Arch Appl Mech.* 80:569–580.
- Haralick RM. 1979. Statistical and structural approaches to texture. *Proc IEEE.* 67:786–804.
- Haralick RM, Shanmugam K, Dinstein I. 1973. Textural features for image classification. *IEEE Trans Syst Man Cybern.* 3:610–621.
- Janse MJ, Ophof T, Kleber AG. 1998. Animal models of cardiac arrhythmias. *Cardiovasc Res.* 39:165–177.
- Janse MJ, van Capelle FJ. 1982. Electrotrophic interactions across an inexcitable region as a cause of ectopic activity in acute regional myocardial ischemia. A study in intact porcine and canine hearts and computer models. *Circ Res.* 50:527–537.
- Johnston PR. 2010. A finite volume method for the bidomain equations and their application to modelling cardiac

- ischaemia. *Comput Meth Biomed Eng.* 13:157–170.
- Johnston BM, Johnston PR, Kilpatrick D. 2008. A solution method for the determination of cardiac potential distributions with alternating current source. *Comput Meth Biomed Eng.* 11:223–233.
- Julesz B. 1962. Visual pattern discrimination. *IRE Trans Inform Theory.* 8:84–92.
- Kehat I, Khimovich L, Caspi O, Gepstein A, Shofti R, Arbel G, Huber I, Satin J, Itskovitz-Eldor J, Gepstein L. 2004. Electromechanical integration of cardiomyocytes derived from human embryonic stem cells. *Nat Biotech.* 22:1282–1289.
- Kleber AG, Rudy Y. 2004. Basic mechanisms of cardiac impulse propagation and associated arrhythmias. *Physiol Rev.* 84:431–488.
- Kohl P, Camelliti P, Burton FL, Smith GL. 2005. Electrical coupling of fibroblasts and myocytes: relevance for cardiac propagation. *J Electrocard.* 38:45–50.
- Kotikanyadanam M, Göktepe S, Kuhl E. 2010. Computational modeling of electrocardiograms – a finite element approach towards cardiac excitation. *Int J Num Meth Biomed Eng.* 26:524–533.
- Krinsky VI. 1978. Mathematical models of cardiac arrhythmias. *Pharmacol Therapeut Part B General Syst Pharmacol.* 3:539–555.
- Lammers WJEP, Schalij MJ, Kirchhof CJHJ, Allessie MA. 1990. Quantification of spatial inhomogeneity in conduction and initiation of reentrant atrial arrhythmias. *Am J Physiol.* 259:H1254–H1263.
- Marth A, Martin J. 2004. Stem cells and repair of the heart. *Lancet.* 364:183–192.
- Menasche P, Hagege AA, Vilquin JT, Desnos M, Abergel E, Pouzet B, Bel A, Sarateanu S, Scorsin M, Schwartz K et al., 2003. Autologous skeletal myoblast transplantation for severe postinfarction left ventricular dysfunction. *J Am College Cardiol.* 41:1078–1083.
- Miragoli M, Gaudesius G, Rohr S. 2006. Electronic modulation of cardiac impulse conduction by myofibroblasts. *Circ Res.* 98:801–810.
- Nagumo J, Arimoto S, Yoshizawa S. 1962. Active pulse transmission line simulating nerve axon. *Proc Inst Radio Eng.* 50:2061–2070.
- Patel AN, Geffner L, Vina RF, Saslavsky J, Urschel HC, Kormos R, Benetti F. 2005. Surgical treatment for congestive heart failure with autologous adult stem cell transplantation: a prospective randomized study. *J Thor Cardiovasc Surg.* 130:1631–1638.
- Rohr S, Scholly DM, Kleber AG. 1991. Patterned growth of neonatal rat-heart cells in culture – morphological and electrophysiological characterization. *Circ Res.* 68:114–130.
- Rook MB, van Ginneken AC, de Jonge B, el Aoumari A, Gros D, Jongsma HJ. 1992. Differences in gap junction channels between cardiomyocytes, fibroblasts, and heterogeneous pairs. *Am J Physiol.* 263:959–977.
- Rubinson DA, Dillon CP, Kwiatkowski AV, Sievers C, Yang L, Kopinja J, Rooney DL, Zhang M, Ihrig MM, McManus MT, et al., 2003. A lentivirus-based system to functionally silence genes in primary mammalian cells, stem cells and transgenic mice by RNA interference. *Nat Genet.* 33:401–406.
- Smith JH, Green CR, Peters NS, Rothery S, Severs NJ. 1991. Altered patterns of gap junction distribution in ischemic heart disease. An immunohistochemical study of human myocardium using laser scanning confocal microscopy. *Am J Pathol.* 129:801–821.
- Sundnes J, Lines GT, Mardal KA, Tveito A. 2002. Multigrid block conditioning for a coupled system of partial differential equations modeling the electrical activity in the heart. *Comput Meth Biomed Eng.* 5:397–409.
- Theofilogiannakos EK, Theofilogiannakos GK, Danias PG, Yioultsis TV, Anogeianaki A, Stergiou-Michailidou V, Kallaras K, Xenos T, Anogianakis G. 2002. A semi-automated approach towards generating a three-dimensional mesh of the heart using a hybrid MRI/histology database. *Comput Meth Biomed Eng.* 14:349–358.
- Tsai CF, Tai CT, Hsieh MH, Lin WS, Yu WC, Ueng KC, Ding YA, Chang MS, Chen SA. 2000. Initiation of atrial fibrillation by ectopic beats originating from the superior vena cava: electrophysiological characteristics and results of radiofrequency ablation. *Circulation.* 102:64–74.
- Wenk JF, Eslami P, Zhang Z, Xu C, Kuhl E, Gorman JH, Robb JD, Ratcliffe MB, Gorman RC, Guccione JM. 2011. A novel method for quantifying the *in-vivo* mechanical effect of material injected into a myocardial infarction. *Ann Thorac Surg.* 92: 935–941.
- Whittington RH, Chen MQ, Giovangrandi L, Kovacs GTA. 2006. Temporal resolution of stimulation threshold: a tool for electrophysiologic analysis. *IEEE Eng Med Biol Soc.* 28:3891–3894.
- Whittington RH, Giovangrandi L, Kovacs GTA. 2005. A closed-loop electrical stimulation system for cardiac cell cultures. *IEEE Trans Biomed Eng.* 52:1261–1270.
- Whittington RH, Kovacs GTA. 2008. A discrete-time control algorithm applied to closed-loop pacing of HL-1 cardiomyocytes. *IEEE Trans Biomed Eng.* 55:21–30.
- Wong J, Göktepe S, Kuhl E. 2011. Computational modeling of electrochemical coupling: a novel finite element approach towards ionic models for cardiac electrophysiology. *Comput Meth Appl Mech Eng.* 200:3139–3158.
- Xie Y, Garfinkel A, Camelliti P, Kohl P, Weiss JN, Qu Z. 2009. Effects of fibroblast-myocyte coupling on cardiac conduction and vulnerability to reentry: a computational study. *Heart Rhythm.* 6:1641–1649.
- Zlochiver S, Munoz V, Vikstrom KL, Taffet SM, Berenfeld O, Jalife J. 2008. Electronic myofibroblast-to-myocyte coupling increases propensity to reentrant arrhythmias in two-dimensional cardiac monolayers. *Biophys J.* 95:4469–4480.
- Zucker SW, Terzopoulos D. 1980. Finding structure in co-occurrence matrices for texture analysis. *Comput Graph Img Proc.* 12:286–308.